ADVANCED MATERIALS
www.advmat.de

Evaporated Se_xTe_{1-x} Thin Films with Tunable Bandgaps for Short-Wave Infrared Photodetectors

*Chaoliang Tan, Matin Amani, Chunsong Zhao, Mark Hettick, Xiaohui Song, Der-Hsien Lien, Hao Li, Matthew Yeh, Vivek Raj Shrestha, Kenneth B. Crozier, Mary C. Scott, and Ali Javey**

Semiconducting absorbers in high-performance short-wave infrared (SWIR) photodetectors and imaging sensor arrays are dominated by single-crystalline germanium and III–V semiconductors. However, these materials require complex growth and device fabrication procedures. Here, thermally evaporated Se_xTe_{1-x} alloy thin films with tunable bandgaps for the fabrication of high-performance SWIR photodetectors are reported. From absorption measurements, it is shown that the bandgaps of Se_xTe_{1-x} films can be tuned continuously from 0.31 eV (Te) to 1.87 eV (Se). Owing to their tunable bandgaps, the peak responsivity position and photoresponse edge of Se_xTe_{1-x} film-based photoconductors can be tuned in the SWIR regime. By using an optical cavity substrate consisting of Au/Al_2O_3 to enhance its absorption near the bandgap edge, the $Se_{0.32}Te_{0.68}$ film (an optical bandgap of ≈0.8 eV)-based photoconductor exhibits a cut-off wavelength at ≈1.7 µm and gives a responsivity of 1.5 AW^{-1} and implied detectivity of 6.5×10^{10} cm $Hz^{1/2}$ W^{-1} at 1.55 µm at room temperature. Importantly, the nature of the thermal evaporation process enables the fabrication of $Se_{0.32}Te_{0.68}$-based 42 × 42 focal plane arrays with good pixel uniformity, demonstrating the potential of this unique material system used for infrared imaging sensor systems.

Infrared photodetectors and imaging sensor arrays (for wavelengths over the range 1–14 µm) have been found to be critical in a wide range of applications including night-vision, remote sensing, optical communications, and emerging medical imaging modalities.[1–4] Semiconductors in devices and arrays for the short-wave infrared (SWIR, 1–3 µm) are dominated by single-crystalline germanium (Ge) and III–V semiconductors such as indium gallium arsenide (InGaAs) and indium gallium arsenide phosphide (InGaAsP).[5–7] However, these materials are typically grown by complex methods, including molecular beam epitaxy (MBE) and metal–organic chemical vapor deposition, resulting in complicated manufacturing procedures and subsequent high cost.[8–12] Although evaporated Ge_xSn_{1-x} films have been explored as alternative materials for SWIR photodetectors, their practical applications are limited by the poor device performance, e.g., low specific detectivity.[13–15] Therefore, it remains challenging to develop novel material systems that can combine a simple preparation process and high device performance.

One potential material system that can meet the requirements stated above is tellurium (Te), a material with 1D crystal structure, which has an indirect bandgap around 0.31 eV.[16,17] One of the key merits is that there are no dangling bonds on the edges and surfaces of Te crystal except at termination points of molecular chains,

Dr. C. Tan, Dr. M. Amani, C. Zhao, Dr. M. Hettick, Dr. D.-H. Lien, Dr. H. Li, M. Yeh, Prof. A. Javey
Electrical Engineering and Computer Sciences
University of California at Berkeley
Berkeley, CA 94720, USA
E-mail: ajavey@eecs.berkeley.edu

Dr. C. Tan, Dr. M. Amani, C. Zhao, Dr. M. Hettick, Dr. D.-H. Lien, Dr. H. Li, M. Yeh, Prof. A. Javey
Materials Sciences Division
Lawrence Berkeley National Laboratory
Berkeley, CA 94720, USA

C. Zhao, Dr. X. Song, Prof. M. C. Scott
Department of Materials Science and Engineering
University of California at Berkeley
Berkeley, CA 94720, USA

The ORCID identification number(s) for the author(s) of this article can be found under https://doi.org/10.1002/adma.202001329.

Dr. X. Song, Prof. M. C. Scott
The Molecular Foundry
Lawrence Berkeley National Laboratory
Berkeley, CA 94720, USA

Dr. V. R. Shrestha, Prof. K. B. Crozier
School of Physics
University of Melbourne
Melbourne, VIC 3010, Australia

Prof. K. B. Crozier
Department of Electrical and Electronic Engineering
University of Melbourne
Melbourne, Victoria 3010, Australia

Prof. K. B. Crozier
Australian Research Council (ARC) Centre of Excellence for Transformative Meta-Optical Systems (TMOS)
University of Melbourne
Melbourne, Victoria 3010, Australia

DOI: 10.1002/adma.202001329

since it is a true 1D material which forms a 3D structure through van der Waals bonding of the molecular chains. Therefore, crystalline Te does not suffer from the surface-induced performance degradation commonly observed in conventional III–V semiconductors that requires additional surface passivation to mitigate. Recent studies have demonstrated that solution-synthesized air-stable Te nanoflakes are a promising semiconductor for the fabrication of photoconductors for infrared photodetection, exhibiting good responsivity and specific detectivity.[18,19] Moreover, Te can be deposited as uniform thin films via simple thermal evaporation process,[20,21] which can be used for fabrication of high-performance p-type field-effect transistors and circuits.[22] However, the performance of Te-based photoconductors is ultimately limited by the high dark current induced by the thermal generation originating from its small bandgap. Alloying Te with large bandgap Se (≈1.9 eV) to form Se_xTe_{1-x} alloys is a feasible and effective way to engineer the bandgap, i.e., allowing it assume between that of Te and Se.[23] Importantly, Se_xTe_{1-x} thin films can also be deposited via simple thermal evaporation. However, their optical, electronic, and optoelectronic properties still remain unexplored.[24,25]

In this work, we report Se_xTe_{1-x} thin films thermally evaporated at cryogenic temperature (–110 °C) with tunable bandgaps for the fabrication of high-performance SWIR photodetectors. We perform a systematic study on the optical properties of evaporated Se_xTe_{1-x} thin films. It is found that the bandgaps of Se_xTe_{1-x} are continuously tunable from 0.31 eV (pure Te) to 1.87 eV (pure Se).[26,27] We then explore the composition-dependent electrical properties and spectral photoresponse of Se_xTe_{1-x} films. We fabricate a high-performance SWIR photoconductor based on $Se_{0.32}Te_{0.68}$ thin film (with an optical bandgap of 0.8 eV) with a 50% cut-off wavelength at 1.7 µm and obtain a implied detectivity of 6.5×10^{10} cm $Hz^{1/2}$ W^{-1} at a wavelength of 1.55 µm and at room temperature. Importantly, the nature of the thermal evaporation process enables the scalability of these devices, which we demonstrate through the fabrication of a 42 × 42 focal plane array based on $Se_{0.32}Te_{0.68}$ thin film. We show that this device has excellent pixel uniformity and we demonstrate its use in imaging.

Se_xTe_{1-x} alloys share the same crystal structure as Te,[16] in which Te atoms are partially substituted by Se atoms, as shown in **Figure 1**a. Although this material appears to be layered when viewed from the *x*-axis, the 3D structure can be more clearly understood by viewing it from the *z*-axis (Figure 1a). It can be clearly seen that triangular helical Se/Te atomic chains stack together in a hexagonal array via van

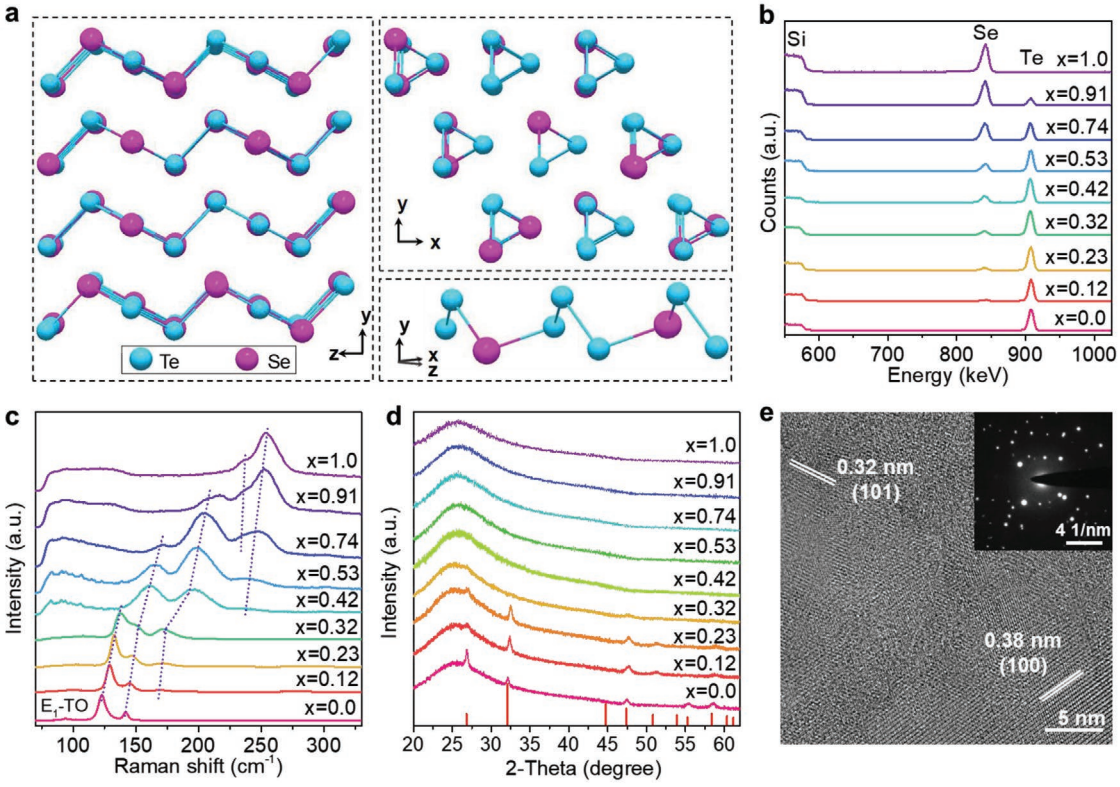

Figure 1. Crystal structure and materials characterization of Se_xTe_{1-x} thin films. a) Crystal structure of Se_xTe_{1-x} crystal viewed from different directions. b) RBS spectra of Se_xTe_{1-x} thin films with different compositions. c) Raman spectra of Se_xTe_{1-x} thin films with different compositions. The Raman spectrum of pure Te film exhibits three peaks, at 93.8, 123.1, and 142.2 cm^{-1}. These correspond to the E_1-TO, A_1, and E_2 modes. Te-like A_1 and E_2 modes gradually shift to greater wavenumbers and a Se-like E_2 mode begins to emerge as Se content increases from 0 to ≈40%. As the Se content increases further, the Te-like A_1 mode disappears, a Se-like A_1 mode emerges, and the ratio of the intensities of the Te-like E_2 mode and the Se-like E_2 mode gradually changes. The Raman spectrum of Se exhibits two peaks at 236.3 and 254.2 cm^{-1}, corresponding to E_2 and A_1 modes. d) XRD patterns of evaporated Se_xTe_{1-x} thin films with different compositions on quartz (the film thickness is within 40–60 nm). e) HRTEM image of an annealed 25 nm thick $Se_{0.32}Te_{0.68}$ thin film. Inset shows the corresponding SAED pattern.

der Waals forces. One of the unique advantages of this material is that Se/Te atoms only connect to two nearest neighbor Se/Te atoms via covalent bonds in each single helical chain (Figure 1a), indicating that Se_xTe_{1-x} has a true 1D crystal structure. Dangling bonds only thus exist at molecular chain terminals in this crystal. Surface recombination is therefore small by comparison to conventional 3D crystals (such as Ge, InGaAs, and InGaAsP)[5–7] and layered 2D crystals (such as black phosphorous, $PtSe_2$ and $PdSe_2$).[28–31]

The Se_xTe_{1-x} evaporation sources are prepared with different chemical compositions (from pure Se to pure Te) by reacting elemental Se shots and Te powders with the desired elemental ratio in a sealed quartz tube at 560 °C overnight (Figure S1a, and Methods of the Supporting Information for details). The X-ray powder diffraction (XRD) peaks gradually shift to greater angles with increasing Se content in Se_xTe_{1-x} crystals (Figure S1b,c, Supporting Information), confirming the formation of alloy crystals. The XRD peak shift is attributed to the change of lattice interlayer spacing induced by substituting Te with Se atoms. Such behavior is consistent with Vegard's law for other solid solutions like $MoS_{2x}Se_{2(1-x)}$ and $Mo_xW_{1-x}S_2$, which have been previously reported in the literature.[32]

These as-prepared Se_xTe_{1-x} alloy crystals are then used as sources to deposit Se_xTe_{1-x} films with varying thickness through a thermal evaporation process at a substrate temperature around –110 °C. The compositions of evaporated Se_xTe_{1-x} thin films are characterized by Rutherford backscattering spectrometry (RBS), as shown in Figure 1b. Quantitative analysis of the RBS results suggests that there is always more Se (≈10–20%) in evaporated Se_xTe_{1-x} thin films than that of the Te source crystal (Figure S2, Supporting Information). This phenomenon can be explained by the fact that the vapor pressure of Se (≈0.14 mmHg at 300 °C) is much higher than that of Te (≈2.5×10^{-4} mmHg at 300 °C) at the same temperature. This leads to the evaporation of Se being faster than that of Te during the thermal evaporation process. The Se_xTe_{1-x} films are also characterized by Raman spectroscopy, further demonstrating the gradual transition from Te to Se (Figure 1c).[16,33] The crystal structures of as-evaporated Se_xTe_{1-x} films are characterized by XRD. It was found that only a few as-prepared high-Te content samples including Te, $Se_{0.12}Te_{0.88}$, and $Se_{0.23}Te_{0.77}$ are polycrystalline (showing peaks in XRD patterns), with the others being amorphous (no peaks in XRD patterns) (Figure 1d). Similar to the source crystals, the XRD peaks of $Se_{0.12}Te_{0.88}$ and $Se_{0.23}Te_{0.77}$ slightly shift to angles greater than those of pure Te. Note that amorphous Se_xTe_{1-x} ($x > 0.3$) thin films can readily be transformed into polycrystalline films through a simple annealing process at mild temperatures (100–140 °C) in a few minutes. It is important to note that for mobile atoms such as Te, the substrate temperature is a critical factor to the film quality. For example, the grain size of an evaporated Te thin film strongly depends on the deposition temperature and maximum grain size can be obtained at cryogenic temperatures. For the case of Se_xTe_{1-x} film evaporated on a low temperature substrate is initially amorphous, the film can be easily transformed into polycrystalline film with relatively large grain size (few micrometers) via mild thermal annealing.[22] Further results on film characterization before and after annealing are shown in Figure S3 of the Supporting Information. The high-resolution transmission electron microscopy (HRTEM) image clearly shows the polycrystalline structure of the annealed $Se_{0.32}Te_{0.68}$ film (Figure 1e). The measured lattice fringes are 0.38 and 0.32 nm, which can be assigned to the (100) and (101) planes of $Se_{0.32}Te_{0.68}$ crystal, respectively. The corresponding selected-area electron diffraction (SAED) pattern shows a few sets of diffraction spots (inset in Figure 1e), further indicating its polycrystalline structure.

We next perform systematic optical characterization of Se_xTe_{1-x} thin films that are evaporated on quartz ($x > 0.3$) or CaF_2 ($x < 0.3$) substrates. Transmission and reflection spectra of Se_xTe_{1-x} thin films are shown in Figure S4 of the Supporting Information. As shown in **Figure 2**a, the composition-dependent absorption spectra of Se_xTe_{1-x} thin films cover a broad wavelength range from the mid-wave infrared (pure Te) to visible (pure Se). The pure Te and Se films have absorption edges around 4000 and 650 nm, respectively, and the absorption edge gradually shifts from 4000 nm to shorter wavelengths when the Se content increases. We then extract the optical bandgaps of Se_xTe_{1-x} films based on the absorption through Cody plots (Figure S5, Supporting Information). Figure 2b clearly shows that the bandgap of Se_xTe_{1-x} thin films can be tuned from 0.31 eV (for pure Te) to 1.87 eV (for pure Se) by

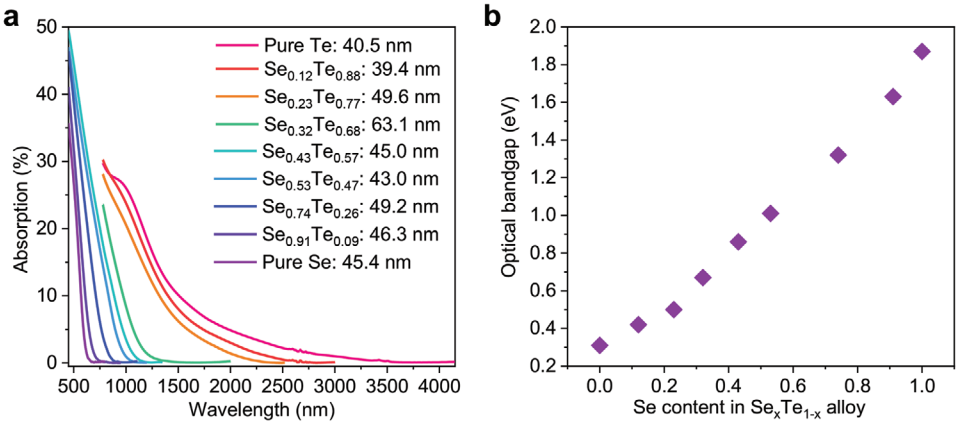

Figure 2. Composition-dependent optical properties. a) Absorption spectra of Se_xTe_{1-x} thin films of various compositions, as calculated from the reflection and transmission measurements. b) Optical bandgaps extracted from the absorption spectra shown in (a).

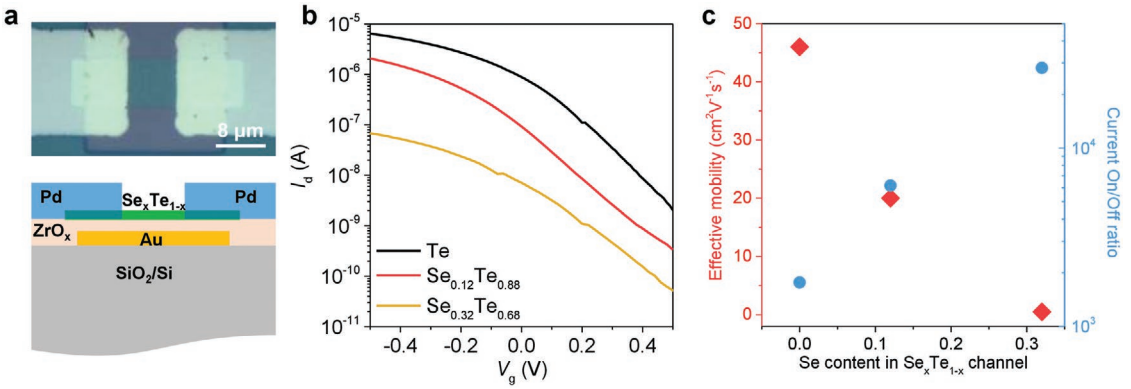

Figure 3. Composition-dependent electrical properties. a) Optical microscopy image and device structure schematic of a Se_xTe_{1-x} film-based FET. b) I_d–V_g curves for Se_xTe_{1-x} FETs with different compositions. c) Effective mobilities and current on/off ratios for Se_xTe_{1-x} film-based FETs with different compositions.

increasing the Se content. Note that all measured samples are indirect bandgap semiconductors.

We next explore the composition-dependent electrical properties of Se_xTe_{1-x} films. The results of Hall effect measurement are summarized in Table S1 of the Supporting Information. The pure Te film gives a Hall effect mobility of 191.2 ± 0.4 cm^2 V^{-1} s^{-1} and hole concentration of 2.6 ± 0.2 × 10^{18} cm^{-3}. However, $Se_{0.12}Te_{0.88}$ gives a Hall effect mobility of 32.3 ± 1.0 cm^2 V^{-1} s^{-1} with a hole concentration of 1.1 ± 0.2 × 10^{18} cm^{-3}. Further increasing the Se content in the Se_xTe_{1-x} films further decreases the Hall effect mobility and hole concentration. We then explore the electrical properties of Se_xTe_{1-x} film-based field-effect transistors (FETs). Back-gated FETs are fabricated using Au as the local back gate, 5 nm ZrO_x as the gate dielectric, Pd as source/drain contacts, and the Se_xTe_{1-x} film as the semiconductor channel. An optical microscopy image and a schematic of the device structure are shown in **Figure 3**a. The I_d–V_g curves clearly show the p-type transport properties for all Se_xTe_{1-x} FETs (Figure 3b). The I_d–V_d curves show Ohmic contact behavior for Se_xTe_{1-x} FETs with a Pd source/drain (Figure S6, Supporting Information). Therefore, we utilize the square law model to calculate the effective mobility (μ_{eff}) in this device as a function of gate field using

$$\mu_{\text{eff}} = \left(\frac{dI_d}{dV_d}\right)\left[\frac{L}{W\left(C_{ox}\left(V_g - V_t - 0.5V_d\right)\right)}\right] \quad (1)$$

where C_{ox} is the gate capacitance, V_t is the threshold voltage, and L and W are the channel length and width, respectively. As shown in Figure 3c, the FET that is based on pure Te with a thickness of 8.5 nm has an effective mobility of ≈46 cm^2 V^{-1} s^{-1} and an on/off ratio of ≈10^3. The effective mobility decreases from ≈46 to ≈1.2 cm^2 V^{-1} s^{-1} when the Se content in the Se_xTe_{1-x} channel increases from 0% to 32%, due to the transition from a crystalline phase to an amorphous phase (Figure 1d), which show the same trend with the Hall effect measurements. The on/off ratio increases from ≈10^3 to more than 10^4, due to the fact that the bandgap increases with Se content (Figure 3c). Note that the electrical properties based on the FETs show the same trend with the Hall effect measurements. Interestingly, the FET based on a much thicker $Se_{0.32}Te_{0.68}$ film (≈22.2 nm) still gives an on/off ratio ≈3.5 × 10^3 and the effective mobility increases to be ≈14 cm^2 V^{-1} s^{-1} (Figure S7, Supporting Information). The high on/off ratio of thick Se_xTe_{1-x} films is favorable for photoconductors, as it means that strong optical absorption and low dark current can be simultaneously achieved.

We next fabricate Se_xTe_{1-x} photoconductors using Au/Al_2O_3 as the substrate (device structure shown in **Figure 4**a). Au finger contacts are used to facilitate efficient electron/hole extraction. An optical microscopy image of a fabricated device is shown in Figure 4b (inset). We next explore the composition-dependent photoresponse of photoconductors based on Se_xTe_{1-x} films. As shown in Figure 4b, these have tailorable spectral photoresponse, achieved by varying the composition and thus the bandgap of the Se_xTe_{1-x}. It can be seen from Figure 4b that the photoresponse edge can be tuned to longer wavelengths by decreasing the Se content. Indeed, it takes values of 1.5, 1.8, and 2.5 μm when the Se content (of the Se_xTe_{1-x} film) is 43%, 32%, and 23%, respectively. Se_xTe_{1-x} thin films thus have widely tunable bandgaps, allowing us to select the photoresponse edge appropriate for the application intended for a given device. To this end, the $Se_{0.32}Te_{0.68}$ thin film with an optical bandgap of 0.8 eV is selected for the fabrication of photodetectors to target SWIR with a cut-off wavelength around 1.7 μm, a typical value for single-crystalline Ge SWIR photodetectors. It is worth to the broad subgap absorption could be attributed to defects in the $Se_{0.32}Te_{0.68}$ film. We therefore use an optical cavity substrate, consisting of an Au back reflector and an Al_2O_3 dielectric spacer, to significantly enhance the absorption in the $Se_{0.32}Te_{0.68}$ film in the shortwave regime (see Figures S8 and S9 of the Supporting Information for the cavity design).[18] In order to achieve optimal performance, we need to strike a balance between the absorption and dark current since both will affect the key figure of merit of photodetectors, i.e., D^*. This leads us to employ $Se_{0.32}Te_{0.68}$ thin films with a thickness of around 28 nm in the devices we next fabricate. The measured absorption of a 23 nm Se_xTe_{1-x} film at 1500 nm is ≈1% (Figure S9d, Supporting Information), which is consistent with the simulated value and the value estimated from ellipsometry measurement simply using Beer's law. To enhance the absorption of

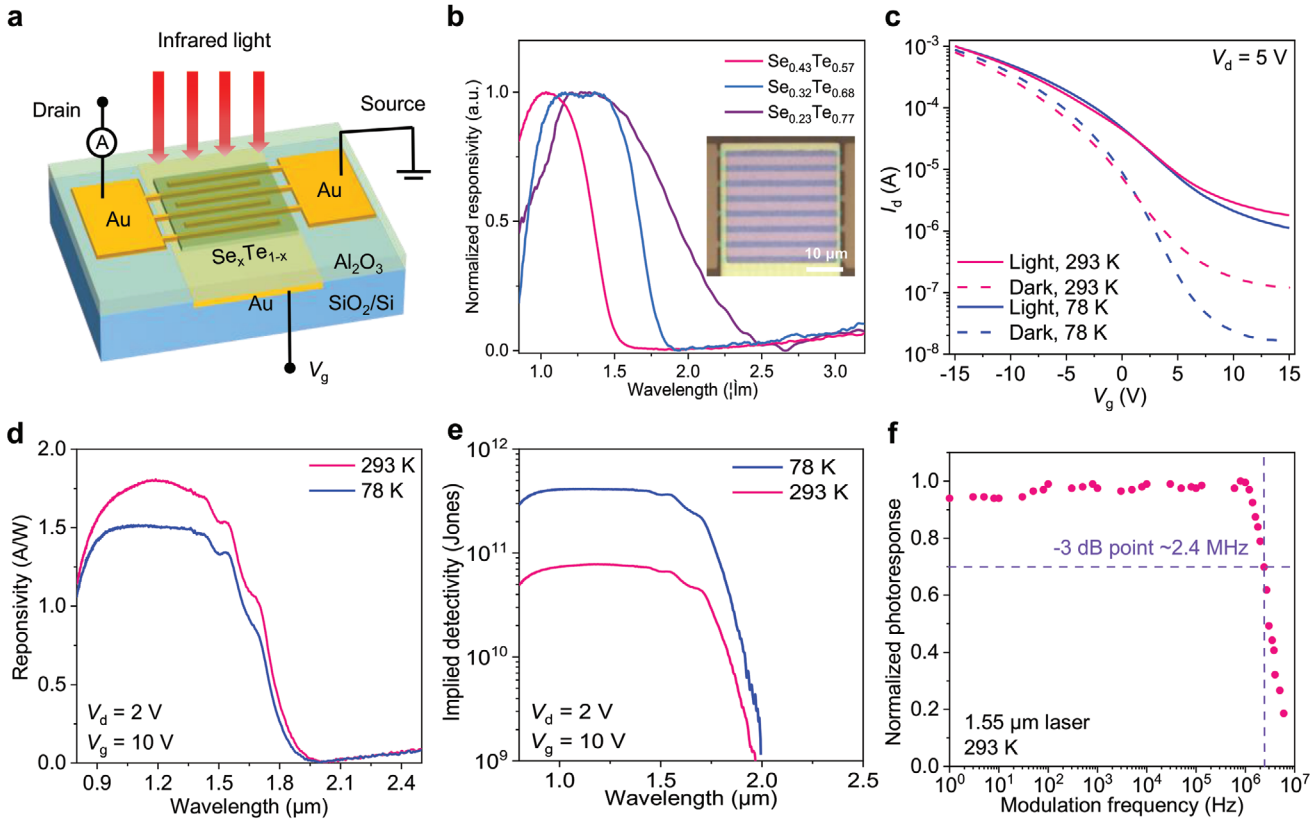

Figure 4. Se_xTe_{1-x} thin-film-based photoconductors. a) Schematic of photoconductor-based on Se_xTe_{1-x} thin film on an Au/Al_2O_3 substrate. b) Normalized spectral responsivity of Se_xTe_{1-x} film-based photoconductors of different compositions. The inset in (b) is the optical microscopy image of Se_xTe_{1-x} thin-film-based photoconductor. c) I_d–V_g characteristics of a photoconductor based on 28 nm thick $Se_{0.32}Te_{0.68}$ at 297 and 78 K in the dark and under illumination. d) Spectral responsivity per watt of a $Se_{0.32}Te_{0.68}$ photoconductor measured at 78 K and 297 K with V_g = 10 V and V_d = 2 V. e) Implied detectivity of $Se_{0.32}Te_{0.68}$ photoconductor. f) Frequency response of $Se_{0.32}Te_{0.68}$ photoconductor showing a 3 dB frequency of 2.4 MHz (λ = 1.55 μm).

the Se_xTe_{1-x} film, an optical cavity substrate consisting of an Al_2O_3 spacing layer and Au back reflector is employed. To find the optimal Al_2O_3 thickness, we perform a simulation of the optical absorption of this film (28 nm thick $Se_{0.32}Te_{0.68}$) on the optical cavity substrate as a function of wavelength and Al_2O_3 thickness (Figure S9c, Supporting Information). Based on these results, we choose the Al_2O_3 film to have a thickness of 75 nm, to enhance the absorption of the $Se_{0.32}Te_{0.68}$ film near its band edge, with the wavelength of peak absorption being 1.5 μm. Note that the optical cavity can also acts as the gate stack for the fabricated photoconductor.

Photocurrent can be observed from the I_d–V_g curves of a typical $Se_{0.32}Te_{0.68}$ photoconductor taken in the dark and under illumination by a white light source at 297 and 78 K, respectively (Figure 4c). The spectral response of the device is then measured via Fourier transform infrared spectroscopy (FTIR) by illuminating the device with the FTIR light source. The intensity versus wavelength of the illuminating light is determined by the internal deuterated triglycine sulfate detector of the FTIR and by a NIST traceable Ge photodiode (see details in Methods of the Supporting Information and ref. [34]). The responsivity (R) of the photoconductor is then calculated through $R(\lambda) = I_{ph}(\lambda)/P_{in}(\lambda)$, where I_{ph} is the photocurrent and P_{in} is the optical power incident on the device. The drain bias-dependent responsivity and D^* of the device at an incident wavelength of 1.4 μm are shown in Figure S10a,b of the Supporting Information. The full spectral responsivity of the device is shown in Figure 4d. For V_d = 2 V and V_g = 10 V, this detector shows a peak responsivity at λ = 1.2 μm of 1.5 and 1.8 AW^{-1} at 78 and 297 K, respectively. We then calculate the detectivity of this device using

$$D^* = \frac{\sqrt{A\Delta f}}{\mathrm{NEP}} = \frac{R\sqrt{A\Delta f}}{i_n} \quad (2)$$

where A is the detector area, NEP is noise equivalent power, Δf is the bandwidth associated with the integration time, and i_n is the noise current.[35,36] The major noise sources are the shot noise $2q(I_p + I_{dark})\Delta f$ and thermal noise $\frac{4k_BT}{R}\Delta f$. To obtain NEP, we first estimate the I_p from

$$\mathrm{SNR} = \frac{I_p^2}{2q(I_p + I_{dark})\Delta f + \frac{4k_BT}{R_{resistance}}\Delta f} \quad (3)$$

All the values are acquired from experimental data, where $R_{resistance} = V_d/(I_p + I_{dark})$, Δf = 2.4 MHz (Figure 4f), and $I_{dark} = 10^{-7}$ A (V_d = 5 V; V_g = 10 V). Under the condition

of SNR = 1, we obtain NEP $= \frac{I_p}{R_\lambda} = 1.6 \times 10^{-7}$ W which yields $D^* = \frac{\sqrt{A\Delta f}}{\text{NEP}} = 3.1 \times 10^{10}$ cm Hz$^{1/2}$ W^{-1}. The implied detectivity as a function of wavelength is shown in Figure 4e for both 78 and 297 K. The device shows a peak D^* of 6.5×10^{10} cm Hz$^{1/2}$ W^{-1} at room temperature. This value increases to a peak value of 3.6×10^{11} cm Hz$^{1/2}$ W^{-1} at low temperatures because the noise current decreases strongly while the responsivity decreases only slightly. To characterize the frequency response, the photoresponse is measured by modulating the laser diode in a sinusoidal manner over a wide frequency range (1 Hz to 8 MHz). As shown in Figure 4f, over this measured spectral range a clear cutoff frequency of ≈2.4 MHz can be seen. We anticipate that this would be more than sufficient for many SWIR applications, e.g., imaging.

The deposition of the $Se_{0.32}Te_{0.68}$ film via a simple thermal evaporation process allows for the wafer-scale deposition of uniform thin films on various substrates. This, combined with the excellent photodetector performance, makes the $Se_{0.32}Te_{0.68}$ film a promising candidate for fabrication of infrared image sensors, such as focal plane arrays (FPAs). To this end, we demonstrate the fabrication of a 42 pixel × 42 pixel FPA using a $Se_{0.32}Te_{0.68}$ film with a thickness of 18.4 nm. The latter is determined by AFM imaging (Figure S11, Supporting Information). **Figure 5**a shows optical microscopy images of the fabricated 42 × 42 FPA obtained at different magnifications. Each pixel has an extent of 80 µm × 90 µm and a structure that is schematically illustrated as Figure 5b. Each pixel has spectral responsivity similar to that discussed previously for the isolated photoconductors

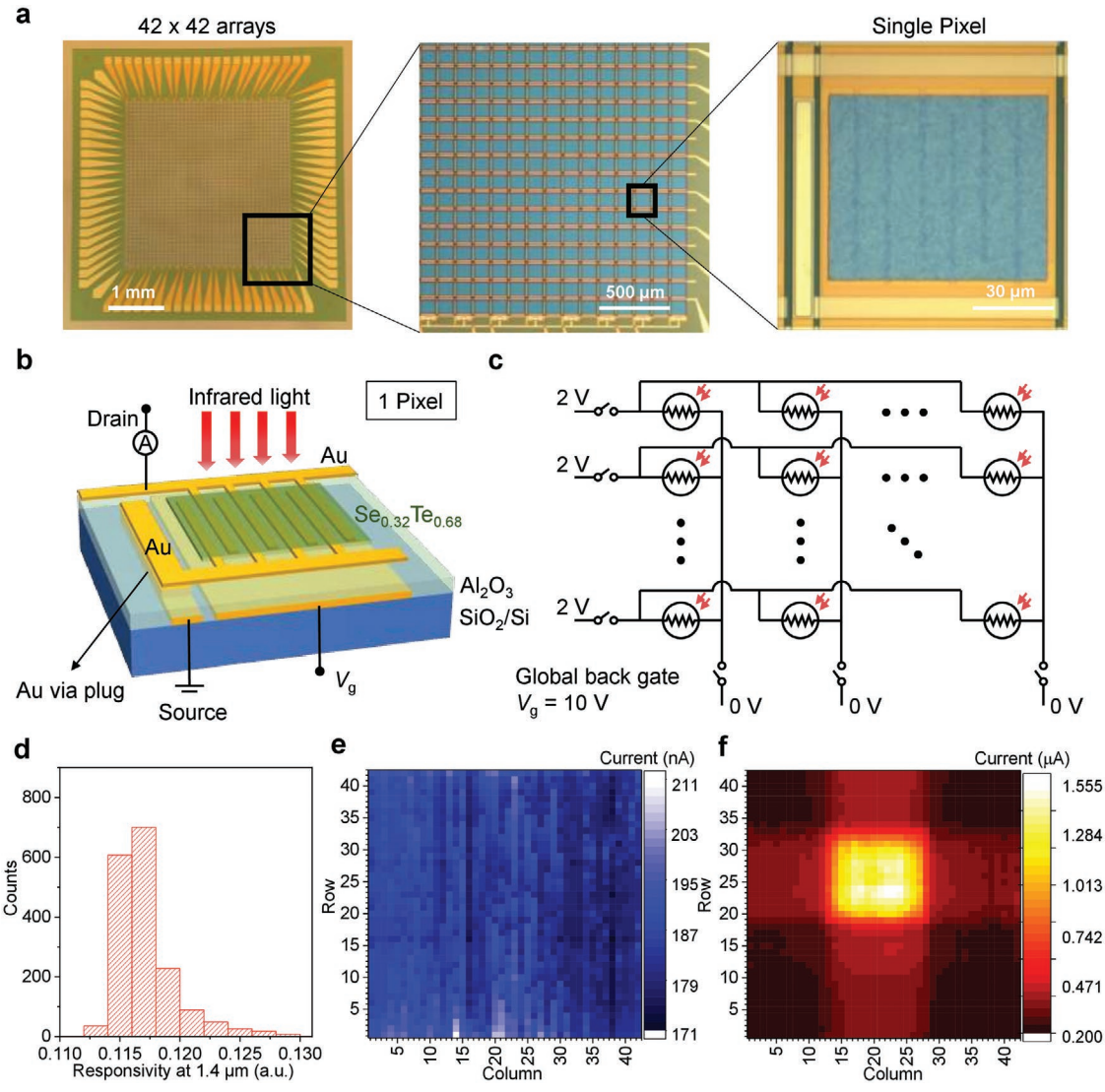

Figure 5. $Se_{0.32}Te_{0.68}$ thin-film-based focal plane arrays. a) Optical microscopy images of 42 pixel × 42 pixel FPA with 1764 pixels at different magnifications. b) Schematic showing the device structure of a pixel. c) Configuration of the passive matrix addressing. Gate voltage is applied (V_g = 10 V) to achieve optimal photodetector performance. Note that a negative gate voltage (V_g = 10 V) is applied when the device is off to reduce the effect of threshold voltage drift. d) Histogram of responsivity (arbitrary units) at 1.4 µm of all 1764 pixels of FPA. e) Dark-current image of FPA. f) Image of white light source of our FTIR taken by the FPA. The image is formed using a camera lens.

(Figure 4d). In order to examine the pixel-to-pixel uniformity of the FPA, we measure both the photoresponse and dark current of all 1764 pixels using a serial passive matrix configuration (Figure 5c). To quantify the FPA uniformity, we present a histogram of the measured responsivities of the pixels at a wavelength of 1.4 μm as Figure 5d. It can be seen that these responsivities have a relatively narrow distribution, indicating that the FPA has good uniformity. Moreover, the FPA also shows a good uniformity in terms of dark current, with the 1764 pixels of the FPA exhibiting dark currents within the range of 170–220 nA (Figure 5e). Furthermore, from these measurements we verify that all 1764 fabricated pixels in the FPA are fully functional, i.e., the die yield is 100%. To demonstrate imaging, we use a camera lens to image the white light source of the FTIR onto the FPA (Figure 5f). Given the simple deposition method and low cost, $Se_{0.32}Te_{0.68}$ thin films have great potential for the construction of high-performance, low-cost, and high-resolution infrared image sensor systems by integrating them with complementary metal–oxide–semiconductor (CMOS) readout chips.[37]

In summary, we have performed a systematic study of the electronic and optical properties of thermally evaporated Se_xTe_{1-x} thin films. We have demonstrated that tunable bandgap Se_xTe_{1-x} alloys are promising materials for the fabrication of high-performance and low-cost SWIR photodetectors. The simple low temperature deposition (–110 °C) of uniform thin films via thermal evaporation also enables the fabrication of FPAs for SWIR imaging. In the future, further refinements in crystallinity and purity could be used to optimize the photodetector performance. In addition, integration of Se_xTe_{1-x} based photodiodes with Si CMOS readout integrated circuits will enable the construction of high-performance, low-cost, and high-resolution SWIR imaging sensor arrays.[37]

Supporting Information

Supporting Information is available from the Wiley Online Library or from the author.

Acknowledgements

C.T. and M.A. contributed equally to this work. Device fabrication and measurements were supported by the Defense Advanced Research Projects Agency under Contract No. HR0011-16-1-0004. Synthesis work was supported by the U.S. Department of Energy, Office of Science, Office of Basic Energy Sciences, Materials Sciences and Engineering Division under Contract No. DE-AC02-05CH11231 within the Electronic Materials Program (KC1201). Work at the Molecular Foundry was supported by the Office of Science, Office of Basic Energy Sciences, of the U.S. Department of Energy under Contract No. DE-AC02-05CH11231. The authors also thank Dr. Yeonbae Lee for his kind help on the RBS measurements.

Conflict of Interest

The authors declare no conflict of interest.

Keywords

focal plane arrays, photodetectors, Se_xTe_{1-x} thin films, short-wave infrared, tunable bandgaps

Received: February 25, 2020
Revised: June 30, 2020
Published online: August 9, 2020

[1] R. F. Potter, W. L. Eisenman, *Appl. Opt.* **1962**, *1*, 567.
[2] A. Rogalski, *Infrared Phys. Technol.* **2007**, *50*, 240.
[3] A. V. Barve, S. J. Lee, S. K. Noh, S. Krishna, *Laser Photonics Rev.* **2010**, *4*, 738.
[4] A. Rogalski, J. Antoszewski, L. Faraone, *J. Appl. Phys.* **2009**, *105*, 091101.
[5] L. Colace, G. Masini, G. Assanto, *Appl. Phys. Lett.* **2000**, *76*, 1231.
[6] T. Martin, R. Brubaker, P. Dixon, M.-A. Gagliardi, T. Sudol, *Proc. SPIE* **2005**, 5783.
[7] C. Cremer, N. Emeis, M. Schier, G. Heise, G. Ebbinghaus, L. Stoll, *IEEE Photonics Technol. Lett.* **1992**, *4*, 108.
[8] M. Oehme, J. Werner, M. Kaschel, O. Kirfel, E. Kasper, *Thin Solid Films* **2008**, *517*, 137.
[9] P. Franzosi, G. Salviati, F. Genova, A. Stano, F. Taiariol, *Mater. Lett.* **1985**, *3*, 425.
[10] M. A. Putyato, V. V. Preobrazhenskii, B. R. Semyagin, Y. B. Bolkhovityanov, A. M. Gilinsky, A. K. Gutakousky, M. A. Revenko, O. P. Pchelyakov, D. F. Feklin, *J. Cryst. Growth* **2003**, *247*, 23.
[11] J. J. Coleman, R. M. Lammert, M. L. Osowski, A. M. Jones, *IEEE J. Sel. Top. Quantum Electron.* **1997**, *3*, 874.
[12] T. Li, J.-F. Cheng, X.-M. Shao, H.-H. Deng, Y. Chen, H.-J. Tang, X. Li, H.-M. Gong, *Proc. SPIE* **2012**, *8419*, 841907.
[13] V. Sorianello, A. De Iacovo, L. Colace, A. Fabbri, L. Tortora, E. Buffagni, G. Assanto, *Appl. Phys. Lett.* **2012**, *101*, 081101.
[14] M. Kim, W. Fan, J.-H. Seo, N. Cho, S.-C. Liu, D. Geng, Y. Liu, S. Gong, X. Wang, W. Zhou, Z. Ma, *Appl. Phys. Express* **2015**, *8*, 061301.
[15] H. Cong, C. Xue, J. Zheng, F. Yang, K. Yu, Z. Liu, X. Zhang, B. Cheng, Q. Wang, *IEEE Photonics J.* **2016**, *8*, 6804706.
[16] Y. Wang, G. Qiu, R. Wang, S. Huang, Q. Wang, Y. Liu, Y. Du, W. A. Goddard, M. J. Kim, X. Xu, P. D. Ye, W. Wu, *Nat. Electron.* **2018**, *1*, 228.
[17] S. Yi, Z. Zhu, X. Cai, Y. Jia, J.-H. Cho, *Inorg. Chem.* **2018**, *57*, 5083.
[18] M. Amani, C. Tan, G. Zhang, C. Zhao, J. Bullock, X. Song, H. Kim, V. R. Shrestha, Y. Gao, K. B. Crozier, M. Scott, A. Javey, *ACS Nano* **2018**, *12*, 7253.
[19] C. Shen, Y. Liu, J. Wu, C. Xu, D. Cui, Z. Li, Q. Liu, Y. Li, Y. Wang, X. Cao, H. Kumazoe, F. Shimojo, A. Krishnamoorthy, R. K. Kalia, A. Nakano, P. D. Vashishta, M. R. Amer, A. N. Abbas, H. Wang, W. Wu, C. Zhou, *ACS Nano* **2020**, *14*, 303.
[20] P. Weimer, *Proc. IEEE* **1964**, *52*, 608.
[21] K. Okuyama, Y. Kumagai, *J. Appl. Phys.* **1975**, *46*, 1473.
[22] C. Zhao, C. Tan, D.-H. Lien, X. Song, M. Amani, M. Hettick, H. Y. Y. Nyein, Z. Yuan, L. Li, M. C. Scott, A. Javey, *Nat. Nanotechnol.* **2020**, *15*, 53.
[23] K. V. Reddy, A. K. Bhatnagar, *J. Phys. D: Appl. Phys.* **1992**, *25*, 1810.
[24] A. M. Ibrahim, L. I. Soliman, *Radiat. Phys. Chem.* **1998**, *53*, 469.
[25] H. El-Zahed, A. El-Korashy, M. Dongol, *Thin Solid Films* **1995**, *259*, 203.
[26] H. Watanabe, K. C. Kao, *Jpn. J. Appl. Phys.* **1979**, *18*, 1849.

[27] A. Mendoza-Galván, E. García-García, Y. V. Vorobiev, J. González-Hernández, *Microelectron. Eng.* **2000**, *51–52*, 677.
[28] H. Yuan, X. Liu, F. Afshinmanesh, W. Li, G. Xu, J. Sun, B. Lian, A. G. Curto, G. Ye, Y. Hikita, Z. Shen, S.-C. Zhang, X. Chen, M. Brongersma, H. Y. Hwang, Y. Cui, *Nat. Nanotechnol.* **2015**, *10*, 707.
[29] J. Bullock, M. Amani, J. Cho, Y.-Z. Chen, G. H. Ahn, V. Adinolfi, V. R. Shrestha, Y. Gao, K. B. Crozier, Y.-L. Chueh, A. Javey, *Nat. Photonics* **2018**, *12*, 601.
[30] X. Yu, P. Yu, D. Wu, B. Singh, Q. Zeng, H. Lin, W. Zhou, J. Lin, K. Suenaga, Z. Liu, Q. J. Wang, *Nat. Commun.* **2018**, *9*, 1545.
[31] G. Zhang, M. Amani, A. Chaturvedi, C. Tan, J. Bullock, X. Song, H. Kim, D.-H. Lien, M. C. Scott, H. Zhang, A. Javey, *Appl. Phys. Lett.* **2019**, *114*, 253102.
[32] C. Tan, W. Zhao, A. Chaturvedi, Z. Fei, Z. Zeng, J. Chen, Y. Huang, P. Ercius, Z. Luo, X. Qi, B. Chen, Z. Lai, B. Li, X. Zhang, J. Yang, Y. Zong, C. Jin, H. Zheng, C. Kloc, H. Zhang, *Small* **2016**, *12*, 1866.
[33] J. Qin, G. Qiu, J. Jian, H. Zhou, L. Yang, A. Charnas, D. Y. Zemlyanov, C. Xu, X. Xu, W. Wu, H. Wang, P. Ye, *ACS Nano* **2017**, *11*, 10222.
[34] M. Amani, E. Regan, J. Bullock, G. H. Ahn, A. Javey, *ACS Nano* **2017**, *11*, 11724.
[35] J. Piotrowski, W. Gawron, *Infrared Phys. Technol.* **1997**, *38*, 63.
[36] J. D. Vincent, *Fundamentals of Infrared Detector Operation and Testing*, Wiley, New York **1990**.
[37] S. Goossens, G. Navickaite, C. Monasterio, S. Gupta, J. J. Piqueras, R. Pérez, G. Burwell, I. Nikitskiy, T. Lasanta, T. Galán, E. Puma, A. Centeno, A. Pesquera, A. Zurutuza, G. Konstantatos, F. Koppens, *Nat. Photonics* **2017**, *11*, 366.